Study of Impact-Induced Mechanical Effects in Cell Direct Writing Using Smooth Particle Hydrodynamic Method

Wei Wang

Yong Huang

Mica Grujicic

Department of Mechanical Engineering,
Clemson University,
Clemson, SC 29634

Douglas B. Chrisey
Department of Materials Science and Engineering,
Rensselaer Polytechnic Institute,
Troy, NY 12180

Biomaterial direct-write technologies have been receiving more and more attention as rapid prototyping innovations in the area of tissue engineering, regenerative medicine, and biosensor/actuator fabrication based on computer-aided designs. However, cell damage due to the mechanical impact during cell direct writing has been observed and is a possible hurdle for broad applications of fragile cell direct writing. The objective of this study is to investigate the impact-induced cell mechanical loading profile in cell landing in terms of stress, acceleration, and maximum shear strain component during cell direct writing using a mesh-free smooth particle hydrodynamic method. Such cell mechanical loading profile information can be used to understand and predict possible impact-induced cell damage. It is found that the cell membrane usually undergoes a relatively severe deformation and the cell mechanical loading profile is dependent on the cell droplet initial velocity and the substrate coating thickness. Two important impact processes may occur during cell direct writing: the first impact between the cell droplet and the substrate coating and the second impact between the cell and the substrate. It is concluded that the impact-induced cell damage depends not only on the magnitudes of stress, acceleration, and/or shear strain but also the loading history that a cell experiences. [DOI: 10.1115/1.2896118]

Keywords: direct writing, cell, hydrogel, impact, smooth particle hydrodynamic method

1 Introduction

Biomaterial direct-write technologies have been receiving more and more attention as rapid prototyping innovations in the area of tissue engineering, regenerative medicine, and biosensor/actuator fabrication based on computer-aided designs (CADs). Direct-write technologies include any techniques or processes capable of depositing, dispensing, or processing different types of materials over various surfaces. During a typical direct-write approach, patterns or layered structures are built directly using a CAD design without the use of masks, allowing rapid prototyping of three-dimensional constructs.

Among the available direct-write technologies, inkjet and laser-based technologies have been most pioneered to precisely position both nonviable and viable biological patterns and construct over different substrates. Successful inkjet printing endeavors include E. coli bacteria [1] and viable mammalian cells [2] deposition using a modified thermal inkjet printer. Laser-based technologies mainly include the use of laser light to form living cell clusters [3], matrix-assisted pulsed-laser evaporation direct write (MAPLE DW) to deposit two-dimensional (2D) [4] and three-dimensional (3D) [5] mammalian cellular structures, and absorbing film-assisted laser-induced forward transfer [6] to assist rat Schwann and astroglial cell deposition. Recently, the electrohydrodynamic jetting (EHDJ) method has been also successfully demonstrated to print viable cells [7]. Using a bottom-up approach, different direct-write methods are envisioned to seed cells and biomolecules to mimic natural tissues, which would yield an enhanced approach for regenerative growth of tissue implants.

In order to commercially implement the different direct-write technologies in the healthcare industry, some biomanufacturing issues need to be carefully addressed. Manufacturing process-induced damage to cells, especially fragile mammalian cells, still poses a significant challenge to achieve a perfect cell viability postcell transfer. For example, cell damage may occur during the cell ejection from supporting media (such as the printer orifice in inkjet printing and the support quartz in MAPLE DW), travel through air, and subsequent impact/collision with the receiving surface in landing, mainly due to the mechanical and thermal effects during cell direct writing. It was found that the transferred cell viability depends on the cell droplet ejection speed and the thickness of substrate culture coating (typically hydrogel-based and used for dual-purpose as cell culture medium and impact cushion) in MAPLE DW, in which cell droplet was ejected from a quartz carrier to a receiving substrate due to the pulsed-laser generated evaporation pressure [4]. High-speed imaging discovered that the velocities of MAPLE DW-ejected material can range from 50 m/s to 1000 m/s [8]. The transferred cells sometimes die if the impact between the cell and the receiving culture coating/substrate during the cell landing leads to cell shear damage including membrane rupture. By assuming the ejection-induced cell damage is negligible, the receiving coating, if necessary, is typically selected based on a trial-and-error approach to avoid the mechanical impact-induced damage. For safe and reproducible cell direct writing, the impact-induced cell damage must be understood in addition to biological property research. It should be pointed out that cell damage during the cell droplet formation and ejection process is also of great concern (both thermomechanical and/or photochemical damage) although it is not of interest in this study.

The objective of this study is to study the cell-substrate hydrogel coating impact-induced mechanical effects in order to better understand the cell mechanical damage during cell direct writing. A previous study has been performed to understand such impact-

Contributed by the Manufacturing Engineering Division of ASME for publication in the JOURNAL OF MANUFACTURING SCIENCE AND ENGINEERING. Manuscript received May 3, 2007; final manuscript received February 10, 2008; published online March 28, 2008. Review conducted by Albert J. Shih.

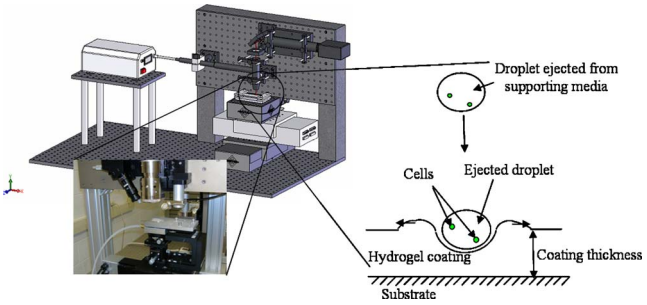

Fig. 1 Schematic of laser-assisted direct writing

induced mechanical effects using an autoadaptive remeshing arbitrary Lagrangian–Eulerian finite element method (FEM) [9]; however, the mesh-based FEM has some difficulties in capturing element distortion due to the possible extremely large deformation of hydrogel, which is typically used as the substrate coating material. To solve the large element distortion challenge in modeling of cell printing process, the smooth particle hydrodynamic (SPH) method, which is mesh-free based, has been used in this study to model large deformations during the cell-hydrogel coating impact process. A dynamics modeling software LS-DYNA [10], incorporated with the SPH method, was used to model the cell impact process of interest.

The paper is organized as follows. First, the SPH computational procedure is introduced. Hydrogel and cell material models are also discussed. Then, the representative simulation results are presented and further discussed to appreciate the mechanical effect of process variables on the cell von Mises stress, vertical acceleration, and maximum shear strain component. Finally, the important conclusions from this study are summarized.

2 Computational Procedure

2.1 Process Governing Equations. The proposed problem is formulated for a generic cell printing process, which can be inkjet-based, laser-assisted, or EHDJ based. The coating material is assumed as a generic hydrogel [9]. Figure 1 depicts a classical print setup and landing process schematic using MAPLE DW. Once a cell droplet, typically enclosed by a hydrogel, is ejected from a supporting medium with an initial velocity, it travels through the air first. Eventually, the cell droplet reaches a receiving substrate, typically a glass slide coated with the hydrogel that allows for cell adhesion and growth and cell impact reduction during landing. This study assumes the cell is uniformly enclosed by the hydrogel to form a droplet, and the receiving substrate coating is also hydrogel based.

During landing, cells undergo significant deceleration and impact(s) and survive a much higher external force than they are capable of under steady state conditions. This landing process and its induced impact can be modeled using the mass, momentum, and energy conservation equations, respectively, as follows:

$$\frac{d\rho}{dt} = -\rho\frac{\partial v_\alpha}{\partial x_\alpha} \tag{1}$$

$$\rho\frac{dv_\alpha}{dt} = \frac{\partial \sigma_{\alpha\beta}}{\partial x_\beta} \tag{2}$$

$$\rho\frac{dE}{dt} = \sigma_{\alpha\beta}\frac{\partial v_\alpha}{\partial x_\beta} \tag{3}$$

where t denotes the time, x is the spatial coordinate, ρ is the density, v_α is the velocity component, $\sigma_{\alpha\beta}$ is the stress tensor component, E is the specific internal energy, and the subscripts α (α=1,2,3) and β (β=1,2,3) are the component indices. The above equations hold true for cells and both hydrogels of the droplet and the substrate coating. Besides boundary and initial conditions, proper material models, which include equation of state, constitutive model, and failure criteria, are also indispensable in solving Eqs. (1)–(3). The equation of state is used to define the corresponding functional relationship between pressure, density, and internal energy. The constitutive model defines the stress dependence of related strain, stain rate, and temperature. In addition, a material model also generally includes a failure criterion to determine whether the material fails and loses its ability to support stress/strain.

2.2 SPH Method. SPH method is a Lagrangian formulation-based computational method (where the coordinates move with the object), which was originally developed for astrophysics and shock simulations [11,12]. After that, it has been applied to various fields, such as hypervelocity deformation [13], detonation [14], and fluid dynamics [15], to name a few.

Using the SPH method, the whole computational domain is divided into a set of discrete particles or nodes. These particles have a spatial distance, known as the smoothing length, over which their properties are smoothed by a kernel function. Different from standard FEM methods, SPH approximates physical quantities of each particle using a kernel function. Smoothing length usually varies in both time and space, and the common kernel functions include the Gaussian function and the cubic spline function. Because it is Lagrangian in nature, SPH is limited to refining based on the particle density alone.

The most attractive feature of this mesh-free SPH method is that it gets rid of the computation termination due to the possible large element distortion inherent in other Lagrangian formulation-based finite element methods. It is expected that SPH can capture the cell-hydrogel coating impact process better.

2.2.1 SPH Approximation. In SPH, the computational domain is first discretized into a finite number of particles. The particle approximation ($\langle f(x)\rangle$) of a function at any spatial coordinate x ($f(x)$) can be represented as follows [15,16]:

$$\langle f(x)\rangle = \int f(x')W(x-x',h)dx' \tag{4}$$

where W is a kernel function, the angular bracket $\langle\ \rangle$ denotes a kernel approximation, h is the smoothing length, which varies in both time and space, x' is new independent variable, and " ′" here and in the following denotes new independent variables.

By introducing a volume weight m^j/ρ^j for each particle, the particle approximation of a function can now be defined by

$$\langle f(x)\rangle = \sum_{j=1}^{N}\frac{m^j}{\rho^j}f(x^j)W(x-x^j,h) \tag{5}$$

where m^j and ρ^j are the mass and density associated with the jth particle, respectively, and N is the number of particles. Thus, the particle approximation for each particle i can be approximated by summing the contributions of neighboring particles j as follows:

$$\langle f(x^i)\rangle = \sum_{j=1}^{N}\frac{m^j}{\rho^j}f(x^j)W(x^i-x^j,h) \tag{6}$$

2.2.2 SPH Formulation. Equations for SPH numerical implementation are constructed by multiplying each term of the exact governing equations (Eqs. (1)–(3)) by the kernel and integrating over the domain where a solution is required. Using the kernel interpolation, the basic SPH mass, momentum, and energy governing equations can be written as follows, respectively:

$$\left\langle\frac{d\rho}{dt}\right\rangle = -\int W\rho'\frac{\partial v'_\alpha}{\partial x'_\alpha}dx' \tag{7}$$

$$\left\langle \frac{dv_\alpha}{dt} \right\rangle = \int W \frac{\partial}{\partial x'_\beta}\left(\frac{\sigma'_{\alpha\beta}}{\rho'}\right)dx' + \int W \frac{\sigma'_{\alpha\beta}}{\rho'^2}\frac{\partial \rho'}{\partial x'_\beta}dx' \tag{8}$$

$$\left\langle \frac{dE}{dt} \right\rangle = \int W \frac{\sigma'_{\alpha\beta}}{\rho'^2}\frac{\partial(\rho' v'_\alpha)}{\partial x'_\beta}dx' - \int W \frac{\sigma'_{\alpha\beta} v'_\alpha}{\rho'^2}\frac{\partial \rho'}{\partial x'_\beta}dx' \tag{9}$$

Then, the finial discrete forms of governing equations can be expressed as follows [16]:

$$\frac{d\rho^i}{dt} = \rho^i \sum_{j=1}^{N} \frac{m^j}{\rho^j}(v^j_\alpha - v^i_\alpha)\frac{\partial W^{ij}}{\partial x^i_\alpha} \tag{10}$$

$$\frac{dv^i_\alpha}{dt} = -\sum_{j=1}^{N} m^j \left(\frac{\sigma^i_{\alpha\beta}}{\rho^{i2}} + \frac{\sigma^j_{\alpha\beta}}{\rho^{j2}}\right)\frac{\partial W^{ij}}{\partial x^i_\beta} \tag{11}$$

$$\frac{dE^i}{dt} = -\frac{\sigma^i_{\alpha\beta}}{\rho^{i2}} \sum_{j=1}^{N} m^j (v^i_\alpha - v^j_\alpha)\frac{\partial W^{ij}}{\partial x^i_\beta} \tag{12}$$

where $W^{ij} = W(x^i - x^j, h)$.

Simulation solutions are obtained by solving Eqs. (10)–(12) in conjunction with material models and initial and boundary conditions.

2.3 Material Models. The complete definition of a transient nonlinear dynamics problem requires the material models that define the relationships among the flow variables (pressure, mass density, energy density, temperature, etc.). These relations typically involve an equation of state, a constitutive equation, and a failure equation for each constituent material. In the present study, the following two materials are utilized within the computational domain: hydrogel (of either the droplet or the substrate coating) and cell. In the following sections, a brief description is given of the models used for hydrogel and cell.

2.3.1 Hydrogel. Natural and synthetic hydrogels contain water within a 3D network of polymer chains [17]. By their nature, hydrogels are highly fluidlike solids, which are water swollen, cross-linked, and hydrophilic polymers. Due to their biocompatibility and the ease of their synthesis, the gels have been extensively used as cell culture and proposed for a wide range of biomedical applications [18,19]. The physical and biochemical properties of a particular hydrogel are highly dependent on its local structure characteristics, constituents and chemical environment, etc. [20,21]. Hydrogel mechanical properties have been of interest for a long time [22,23], and some hydrogel mechanical property characterization studies have been reported [22–24]. However, a complete understanding of hydrogel mechanical properties is still lacking.

The equation of state of hydrogel is expected to provide a hydrodynamic material model by which the hydrogel volumetric strength can be determined. The Mie–Grüneisen equation of state, as shown in Eq. (13) [10], provides the shock velocity-particle velocity Hugoniot form and was used to define the equation of state of hydrogel:

$$P = \frac{\rho_0 C^2 \mu \left[1 + \left(1 - \frac{\gamma_0}{2}\right)\mu - \frac{a}{2}\mu^2\right]}{\left[1 - (S_1 - 1)\mu - S_2\frac{\mu^2}{\mu+1} - S_3\frac{\mu^3}{(\mu+1)^2}\right]} + E_i(\gamma_0 + a\mu) \tag{13}$$

where P is the hydrogel pressure, C is the intercept of the $U_s - U_p$ curve (sound velocity), U_s is the speed of a shock wave through the material, U_p is the speed of the shocked material, S_1, S_2, and S_3 are the coefficients of the slope of the $U_s - U_p$ curve, γ_0 is the Grüneisen gamma, E_i is the internal energy per initial volume, a is the first order volume correction to γ_0, the compression μ is defined as $\mu = \rho/\rho_0 - 1$, and ρ and ρ_0 are the density and initial density. The Mie–Grüneisen equation is typically determined based on the material parameters C, S_1, S_2, S_3, and γ_0 as specified by LS-DYNA [10]. In this study, since water is the dominant component of hydrogel, the parameters for water were used to define the hydrogel equation of state to simplify the problem.

Null material model has been adopted by LS-DYNA to model the fluidlike materials [10]. Since the hydrogel demonstrates fluidlike behavior during large deformation, for simplicity, the null material model provided by the LS-DYNA material library was used as the hydrogel constitutive model. When using the null material model, pressure and deviatoric stress are decoupled in the SPH simulation. The pressure is determined by the equation of state as Eq. (13), and the deviatoric stress is calculated based on the strain rate and viscosity as follows:

$$\sigma^D_{\alpha\beta} = 2\mu_h \dot{\varepsilon}^D_{\alpha\beta} \tag{14}$$

where $\sigma^D_{\alpha\beta}$ is the deviatoric stress, μ_h is the hydrogel viscosity, and $\dot{\varepsilon}^D_{\alpha\beta}$ is the deviatoric strain rate.

Hydrogel loses its mechanical loading bearing capacities under certain stress/strain conditions. As a result, the cell droplet may penetrate into the hydrogel coating during the subsequent processes. Cutoff pressure is used to control the hydrogel failure by allowing the hydrogel to numerically cavitate when the hydrogel undergoes dilatation above a certain magnitude. The pressure information of the landing process can be determined using the hydrogel equation of state.

2.3.2 Cell. During the cell printing process, the cells, which are enclosed by the hydrogel, also undergo complexly dynamic stress and strain variations. Due to the complexity of cell structure and compositions, numerous constitutive models have been developed to characterize mechanical responses of living cells when subjected to both transient and dynamic loads [25]. Generally, cell models can be considered on two levels, macroscopic continuum approaches and microscopic structural approaches. The continuum approach aims to investigate the overall behavior of cells while the microscopic structural approaches focus on the effect from the local component deformation of cells.

The linearly elastic solid cell model was selected in this study due to its simplicity and adequateness. The whole cell is assumed as homogeneous without considering the distinct cortical layer. The linearly elastic solid model is a simplification of the viscoelastic model when the time factor is neglected.

A linearly elastic material can be described as follows by defining $T^D_{\alpha\beta} = T_{\alpha\beta} + p\delta_{\alpha\beta}$ and $\varepsilon^D_{\alpha\beta} = \varepsilon_{\alpha\beta} - \frac{1}{3}e\delta_{\alpha\beta}$ [26]:

$$T^D_{\alpha\beta} = 2G\varepsilon^D_{\alpha\beta} \text{ and } p = -Ke \tag{15}$$

where $T^D_{\alpha\beta}$ are the deviatoric components of stress components $T_{\alpha\beta}$, $\varepsilon^D_{\alpha\beta}$ are the deviatoric components of the strain components $\varepsilon_{\alpha\beta}$, G is the shear modulus, p is the cell mean normal pressure (hydrostatic pressure), $e = \varepsilon_{11} + \varepsilon_{22} + \varepsilon_{33}$ is the volume strain, $\delta_{\alpha\beta}$ is the Kronecker delta, and K is the bulk modulus.

An equation of state is not necessarily required for pressure calculation when using an elastic constitutive model for cells as specified by LS-DYNA. If the pressure information is of interest, the pressure can be computed using the resultant stress tensor information from the constitutive model.

Since the goal of this study is to study the companying cell stress and strain distribution during the dynamic landing process, the cell failure is not of interest here and the predicted stress and strain values are not compared with the failure threshold values of any cells. This study serves as a foundation for future cell damage/failure modeling during cell direct writing.

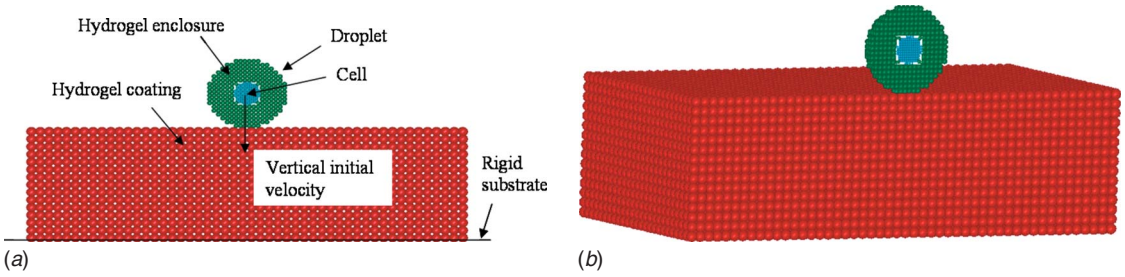

Fig. 2 Illustration of SPH computational modeling domain

3 Simulation Setup and Results

3.1 Mesh-Free Model Setup. As the first step toward cell damage modeling during cell direct writing, this study has only considered the case that there was one cell inside a droplet and the cell was in the middle of the droplet. Once the cell droplet left from the ejecting device, the cell droplet was assumed to impact the hydrogel coating in a normal direction. The initial droplet velocity was the impact velocity when the cell droplet first reached the coating, and the positive velocity direction was defined vertically downward, as shown in Fig. 2.

In a mesh-free method, the particle grid density is crucial for computation implementation. Uniform grid distribution was used in this study. The hydrogel coating bottom was supported by a rigid substrate and modeled as a rigid boundary condition, and the rigid wall model in LS-DYNA was used to model the rigid impact between the particle flow and the rigid substrate body. The rigid wall model was applied to other coating surrounding boundaries in order to limit the particles to flow through since the coating size along the X and Y dimensions (both 100 μm) was considered infinite than that of the cell droplet in this study, and there was negligible differences in simulations when even larger XY dimensions were tested. The coating surface was modeled as a free surface. To reduce the computational cost, a symmetrical plane was used so that a half model was applicable (Fig. 2).

The schematic of the grids implemented is shown in Fig. 2. In total, 20,692 particles are used, in which 456 for the cell, 1486 for the droplet hydrogel, and 18,750 for the hydrogel coating, respectively. The particle numbers were selected based on a modeling accuracy sensitivity study. The smoothing length was selected from 0.8 to 1.0. The hydrogel droplet diameter was assumed 18 μm, and the cell diameter 6 μm [27]. Figure 3 shows the positions of selected particles, which are of interest in the following discussion.

As discussed, the null material model was implemented as the hydrogel constitutive model to model the fluidlike material behavior of hydrogel. The equation of state parameters of water were adopted for hydrogel as $C=1500$ m/s, $S_1=2.56$, $S_2=-1.986$, $S_3=0.2286$, and $\gamma_0=0.5$ [28,29]. The hydrogel initial density was taken as 1000 kg/m^3 and viscosity as 12 cP [20]. The failure cutoff pressure of hydrogel was set as 25 kPa [9]. The density of cell was also assumed 1000 kg/m^3, Young's modulus 1.79 MPa [27], and Poisson's ratio 0.475 for simplicity [9].

3.2 Representative Simulation Results

3.2.1 Evolution of a Landing Process. Some representative simulation results of landing are presented when a 50 m/s (V_0) cell droplet hit a rigid substrate coated with a 30 μm thick hydrogel. Figure 4 shows the evolution of the whole landing process. It can be seen that there were two different impacts during the whole process under the specified conditions. The first impact was between the cell droplet and the hydrogel coating, and the second impact was between the cell and the rigid substrate after the cell passed through the coating after the first impact.

As the landing process went on, the hydrogel-enclosed cell droplet gradually merged into the substrate coating. Before the cell immersed into the coating (Figs. 4(a) and 4(b)), it was the outside hydrogel enclosure that was mainly subjected to the impact-induced stress. It shows that the outside hydrogel enclosure of the cell played an important role in alleviating the impact-induced stress to the cell by absorbing the strain energy. Around 0.1600 μs later, the impact between the cell and the hydrogel coating occurred. After the cell immersed into the coating (Figs. 4(c) and 4(d)), the outside hydrogel enclosure and the coating bore relatively lower stresses although the cell experienced higher stresses.

3.2.2 Von Mises Stress and Shear Strain. To study the von Mises stress and shear strain information during the landing process, three particles, the top particle 19,139, the inner particle 19,144 (one of the four center particles), and the bottom particle

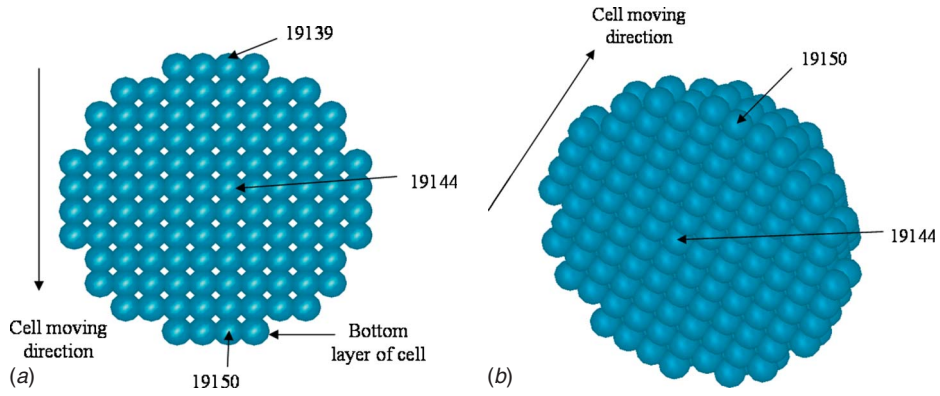

Fig. 3 Distribution of the selected particles in the cell and its 3D visualization

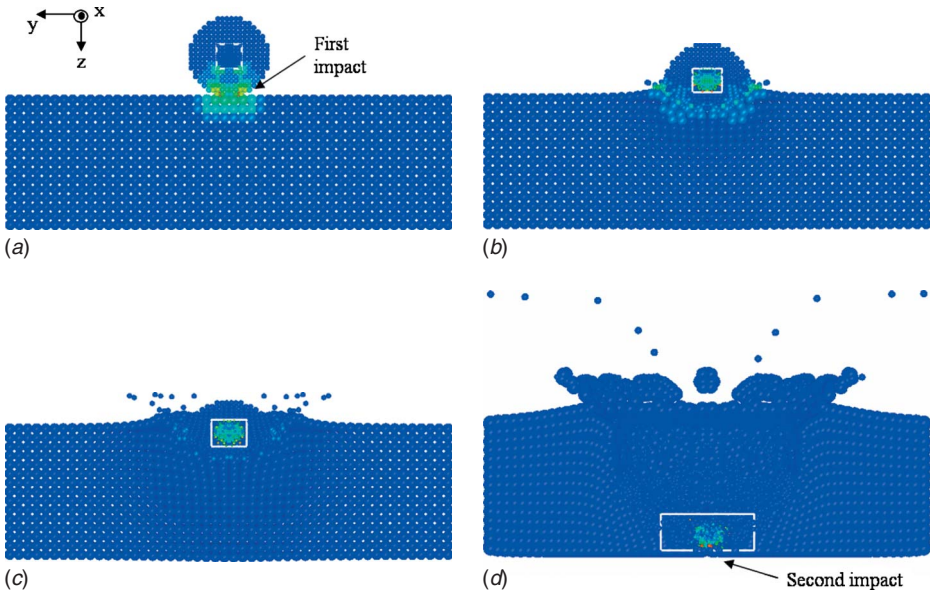

Fig. 4 Landing process at (*a*) 5.9322 ns, (*b*) 0.1359 μs, (*c*) 0.2725 μs, and (*d*) 2.4865 μs

19,150, were selected as the representative positions to better understand the overall cell responses during the landing process. The simulation was performed under the condition of coating thickness=30 μm and V_0=50 m/s.

The particle von Mises stress responses are shown in Fig. 5. It can be seen from the stress profiles that there were two different impacts during the whole process under the specified conditions. The first impact happened at the computation starting time, and the second impact happened around 2.2 μs. The von Mises stress level was comparable with that of a previous study using the arbitrary Lagrangian–Eulerian FEM [9], and both were at the order of 10^5 Pa. During the whole process, the peripheral particles 19,139 (top) and 19,150 (bottom) were subjected to a higher stress level than that of the inner particle 19,144, which indicates that the cell membrane had a higher impact-induced mechanical stress during cell direct writing. Also, the bottom particle 19,150 underwent a higher stress than that of the top particle 19,139. Figure 5 also shows that the second impact had a negligible effect to the particles 19,139 (top) and 19,144 (inner); however, the bottom particle 19,150 had an even higher stresses during the second impact than that during the first impact (1.03 MPa versus 0.96 MPa), which means that it is of importance to study the stress information of the bottom particles during both impacts.

In this simulation, the bottom particle 19,150 experienced the first impact-induced stress peak at 0.2 μs and the second peak around 2.6 μs. It is found that the bottom peripheral particles were easy to have a second impact, followed by the top peripheral particles, and then the inner particles.

Figure 6 shows the maximum shear strain information of the three particles of interest. The maximum shear strain component was found along the YZ direction (ε_{YZ}), as shown in Fig. 4(*a*). It can be seen that the peripheral particles (19,139 and 19,150) had a larger shear deformation, which indicates a good chance of cell membrane to be ruptured during the impact process if the shear strain is the cell failure criterion.

3.2.3 Velocity and Acceleration. The same particles 19,139

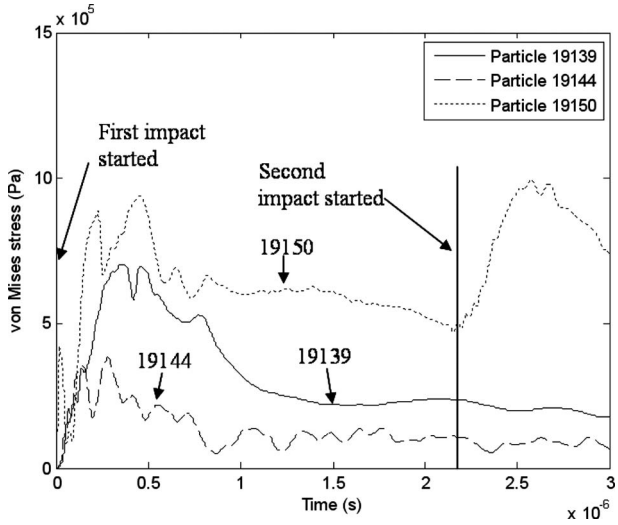

Fig. 5 Particle von Mises stress information (coating thickness=30 μm and V_0=50 m/s)

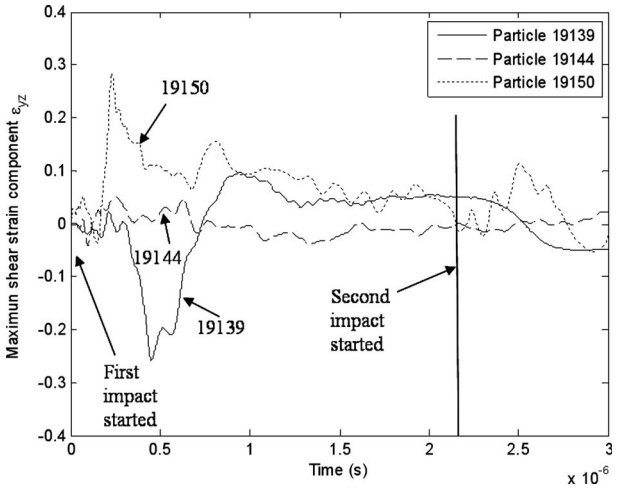

Fig. 6 Particle maximum shear strain component information (coating thickness=30 μm and V_0=50 m/s)

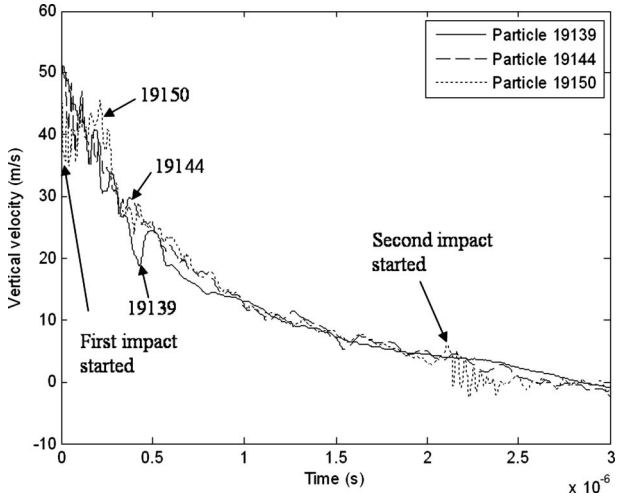

Fig. 7 Particle vertical velocity information (coating thickness=30 μm and V_0=50 m/s)

(top), 19,144 (inner), and 19,150 (bottom) were selected to study their velocity and acceleration responses during the landing process (coating thickness=30 μm and V_0=50 m/s). All velocity and acceleration information here was about their vertical components along the Z direction since the velocity and acceleration at the other directions were relatively small as observed.

Figure 7 shows the velocity history of the three particles until they settled down on the rigid substrate. After the first impact, the bottom particle (19,150) first experienced a velocity decrease, followed by the inner and top particles (19,144 and 19,139). The velocity decrease observed from Fig. 7 was oscillatory because of the material models used (the elasticity of cell and the fluid-type property of hydrogel). It can be seen that the velocity differences at the different positions were relatively larger at the beginning of the landing process, and then the difference smoothed out. The second impact caused an additional velocity oscillation around 2.2 μs, especially to the bottom particle (19,150), which can be further seen from the acceleration profile in Fig. 8. Finally, all particles were still at the end of the landing process.

As seen from Fig. 8, the particle decelerated as high as 10^8–10^9 m/s^2 during cell direct writing, which is consistent with

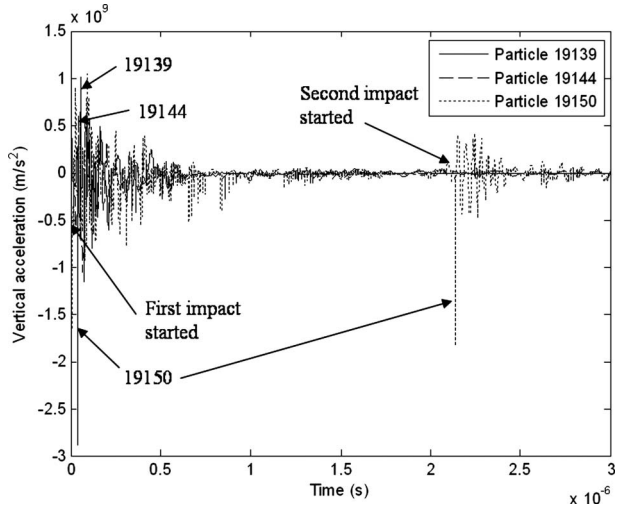

Fig. 8 Particle vertical acceleration information (coating thickness=30 μm and V_0=50 m/s)

a previous FEM study [9] and comparable with other simple estimations (at the order of 10^7 m/s^2) [4]. Generally, the absolute acceleration magnitude became smaller and smaller and eventually approached zero in an oscillation manner. Absolute magnitudes of acceleration depend on the material properties of the hydrogel and the cell, coating thickness, and droplet initial velocity. As discussed before, the bottom particle 19,150 experienced another negative peak of acceleration (deceleration) due to the second impact, which indicates that the bottom particles are easily subjected to the second impact than particles at other positions.

Two conclusions can be drawn based on the above velocity and acceleration simulation. First, relatively larger oscillations of velocity and acceleration are expected at the beginning of the first impact, and the velocity and acceleration differences between different particles smooth out as the landing process goes on. Second, the bottom peripheral cell membrane experiences a higher impact effect than other locations.

3.3 Effect of Process Variables and Discussion. If cell damage during cell direct writing is of interest, the effect of typical process variables, such as the droplet initial velocity and the coating thickness, needs to be carefully studied. For example, the receiving coating, if necessary, has been typically selected based on a trial-and-error approach to avoid mechanical stress-induced damage/necrosis. In this section, the effect of droplet initial velocity and coating thickness on cell stress, acceleration, and shear strain component is investigated and further discussed. Since the bottom particle 19,150 usually underwent relatively severe mechanical loadings compared with particles at other positions as discussed in the above section, it was selected as the representative particle/cell membrane position to be studied.

3.3.1 Effect of Initial Velocity. To study the effect of droplet initial velocity, some typical speed values such as 50 m/s, 100 m/s, and 300 m/s were selected. Figure 9 presents the comparisons of von Mises stress, vertical acceleration, and maximum shear strain component of the bottom particle 19,150 under the three different initial velocities. As expected, the absolute magnitudes of effective stress, vertical acceleration, and maximum shear strain showed a close relationship with the initial velocity. A higher initial velocity led to a higher stress level, larger acceleration, and larger maximum shear strain component. If mechanical damage is of concern, lowering the magnitude of cell droplet ejecting velocity can effectively reduce the mechanical impact on cells, protecting cells from the mechanically induced damage. Therefore, it is important to control the initial velocity within a certain range so that the excessive stress level, large acceleration, and/or large shear strain can be avoided.

3.3.2 Effect of Coating Thickness. To fully understand the effect of coating thickness, some typical coating thickness values such as 0 μm (uncoated), 20 μm, and 40 μm were selected for simulation. Figure 10 presents the comparisons of von Mises stress, vertical acceleration, and maximum shear strain component of the bottom particle 19,150 using the different coating thicknesses.

As expected, the cells experienced significantly higher von Mises stress, vertical acceleration, and maximum shear strain using the uncoated substrate (thickness=0 μm) than those using the coated substrates. Even a thin coating such as a 20 μm thick hydrogel coating helped to reduce the possible mechanical damage by several times. It is seen that the maximum von Mises stress using the uncoated substrate was reduced from 3 MPa to be around 1 MPa using a 20 μm or 40 μm thick coating. Similar protective effect of a coating can also be observed in terms of the vertical acceleration and maximum shear strain component, as seen from Fig. 10. Generally, the mechanical damage to cell can be evaluated based on the criteria of von Mises stress, acceleration, and/or shear strain. Whichever the criterion is to be used, the cell mechanical damage can be reduced and the cell viability can

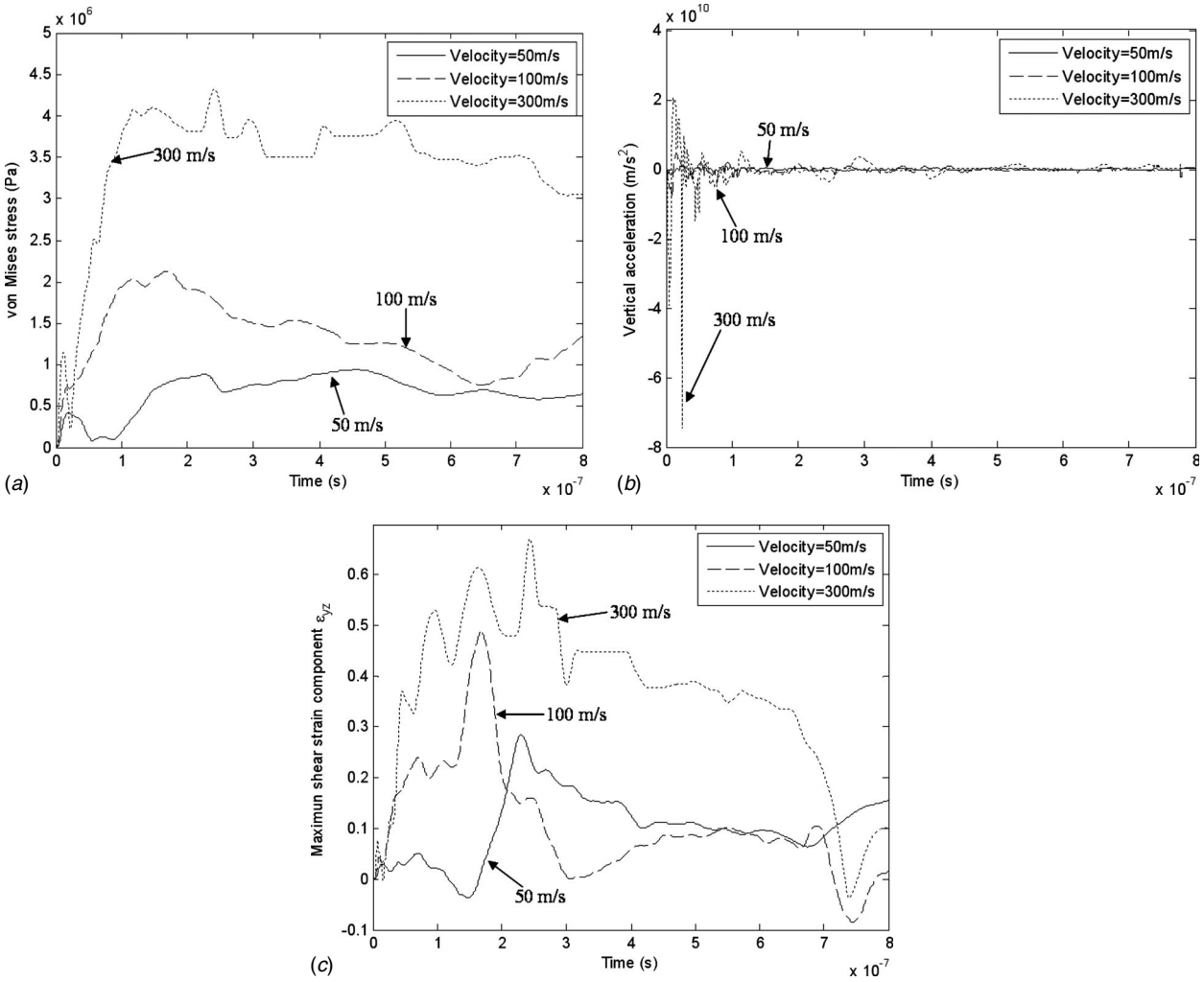

Fig. 9 von Mises stress, vertical acceleration, and maximum shear strain component information of the bottom particle 19,150 at different velocities (coating thickness=30 μm)

be improved using a proper coating, as reviewed from Fig. 10.

The protective effect of coating has been also experimentally verified during laser printing of pluripotent embryonal carcinoma cells [4]. Based on that study, 5% cell viability after printing was achieved using an uncoated quartz receiving substrate; however, roughly 50% of the cells transferred onto a thinner hydrogel coating (20 μm) appeared to remain viable post-transfer, whereas viability reached 95% for cells transferred onto a thicker coating (40 μm). However, by reviewing Fig. 10, it is found that there were no pronounced differences between the maximum von Mises stresses or the maximum shear strain components when using the 20 μm or 40 μm thick coating. If the cell viability is just evaluated based on the maximum von Mises stress or the maximum shear strain component, it is difficult to explain why the 40 μm coating helped achieve almost a doubled cell viability compared with that using the 20 μm coating. The reason that the cell viability was lower using the 20 μm coating is attributed to the second impact between the cell and the rigid substrate around 1.7 μs while there was no pronounced second impact using the 40 μm coating.

3.3.3 Discussion. To further appreciate the effect of droplet initial velocity and coating thickness on maximum von Mises stress and shear strain component during impact, a comparison study has been performed for the bottom particle 19,150 under the different combinations of velocity and coating thickness, and the results are shown in Table 1.

Generally, cell mechanical damage mechanisms can be mitochondria swelling, cell membrane rupture, endoplasmic reticulum dilation, and vacuole formation, which make cells die during cell direct writing. Regarding the maximum von Mises stress, the following can be found from Table 1.

1. While there was no pronounced difference when using a 20 μm or 40 μm thick coating, there was a three times difference between the coated and uncoated cases during the first impact under the investigated velocities.
2. If a thin coating did not provide enough damping during the interaction between the cell droplet and the coating, the second impact might cause an even higher effective stress to the cell especially as seen from the scenario using a 100 m/s velocity and 20 μm coating since the second impact was between the cell and the rigid substrate. Even the cell velocity was lower during the second impact as seen from Fig. 7, and the impact between the cell and the rigid substrate might lead to a higher impact force as a result of the combined effect of velocity and nature of the second impact (the impact with a rigid surface).
3. Although the stress levels were comparable during the first impact for both coated cases, the mechanical damage to cells might be different depending on the following second impact. As discussed in the previous section, when a 20 μm or

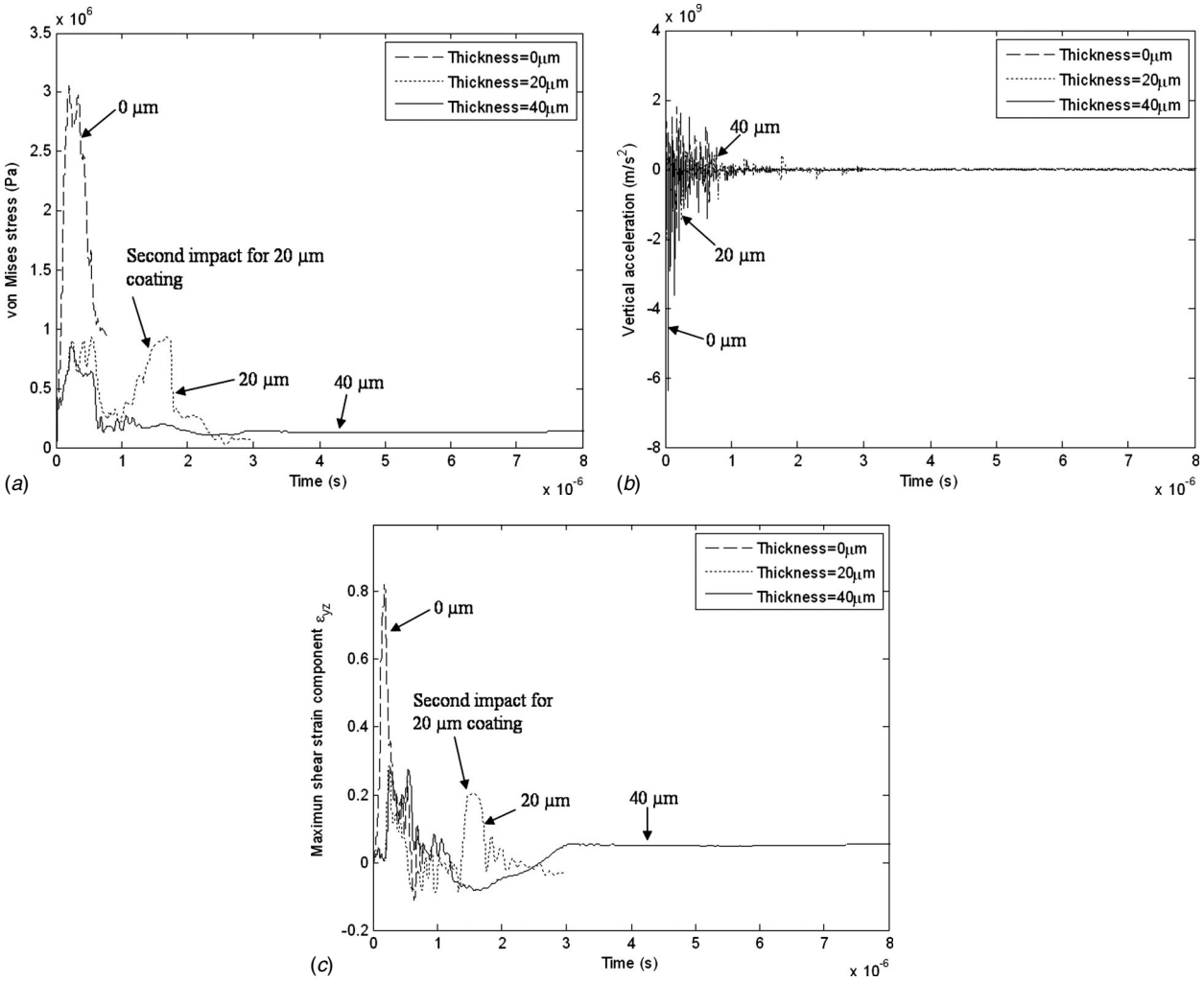

Fig. 10 von Mises stress, vertical acceleration, and maximum shear strain component information of the bottom particle 19,150 at different thicknesses (initial velocity=50 m/s)

40 μm thick coating was used, the first impact-induced stress was found comparable as 0.92 MPa versus 0.86 MPa and 1.90 MPa versus 1.95 MPa; however, the cell viability was 50% versus 95%. It indicates that the stress profile after the first impact and/or the second impact-induced stress peak should also be included to determine the cell post-transfer viability. It is known that the cellular response to mechanical injuries is adaptive to restore a normal homeostasis and protect the cell from progressive damage [30,31]. Cell injury by mechanical trauma is closely related to the mechanical loading method since the cellular response varies according to the method used to induce the mechanical injury [32]. It is assumed that the second impact-induced stress peak may happen before a cell has time to restore homeostasis, which leads to a lower cell post-transfer viability during cell direct writing. The loading history experienced by cells is also critical in determining cell damage. It should be pointed out that the simulation results should adequately represent a general cell droplet landing process for us to draw the above conclusion although the material properties of cell and hy-

Table 1 Maximum von Mises stress and shear strain component information during impacts of the bottom particle 19,150 (NA: not applicable)

Velocity (m/s)	Coating thickness (μm)	Maximum von Mises stress (MPa)		Maximum shear strain component (ε_{YZ})	
		During first impact	During second impact	During first impact	During second impact
50	0	3.05	NA	0.8225	NA
	20	0.92	0.94	0.2884	0.2067
	40	0.86	NA	0.2771	NA
100	0	6.04	NA	0.8401	NA
	20	1.90	2.72	0.5214	0.3886
	40	1.95	1.30	0.5181	0.2646

drogel are not exactly the same as in Ref. [4].

4. Typically, cells such as yeast cells fail mechanically around 70 ± 4 MPa [33], which is one order higher than those predicted in this study. It looks like that fragile mammalian cells die at much lower stress levels during cell direct writing as seen from Table 1. There are two possible reasons for this discrepancy: the pluripotent embryonal carcinoma cell [4] is fragile while the yeast cell is relatively tough; the dynamic mechanical loading makes cells difficult to restore their normal homeostasis [30–32] as discussed before.

Similar magnitude observations/tendencies of the maximum shear strain component have been found while comparing with those of the von Mises stress except that the maximum shear strain component of the second impact (if have) was always smaller than that of the first impact. It should be noted that since the cell failure is not considered here and the predicted stress and strain values were not compared with any failure criteria, some unrealistic shear strains were predicted such as 0.8225 and 0.8401 for the uncoated cases. It is expected that more realistic strain values can be predicted if a cell failure criterion for a certain type cell is implemented in future studies.

It should be pointed out that this simple elastic model is not adequate to study the mechanical response of the different components of the cell. The assumption that the cell is homogenous and behaves in a linear elastic manner ignores a number of potential important features of real cells. Since the general stress and strain information is of interest, this elastic model is sufficient for this preliminary study. A more realistic inhomogeneous, nonlinear cell constitutive model should be considered for landing modeling and cell damage and failure modeling.

In summary, it is assumed that the impact-induced cell damage depends not only on the magnitudes of stress, acceleration, and/or shear strain but also the loading history that a cell experiences. In fact, the collective cell momentum change over the whole impact duration instead of peak values of stress, acceleration, and/or strain looks critical in determining the cell viability during cell direct writing. This loading history-based damage prediction approach should be further carefully addressed in future investigations. It should be noted that once the coating thickness reaches a certain value, there is no extra benefit for mechanical damage-induced cell viability improvement. This critical thickness value depends on the cell droplet initial velocity and the material properties of the cell and the hydrogel.

4 Conclusions

The impact between the cell droplet and the substrate coating and the impact between the cell and the substrate have been carefully studied using a mesh-free SPH method in this study. The effects of cell droplet velocity and coating thickness on the cell stress, acceleration, and shear strain during landing have been carefully investigated and discussed. Some conclusions can be drawn as follows.

1. The cell peripheral regions, especially the bottom peripheral region, usually experience a higher stress level than that of the inner regions. It indicates that the cell membrane is easy to be adversely affected by the impact-induced mechanical damage during cell direct writing.
2. The cell mechanical loading profile and the cell post-transfer viability depend on the cell droplet initial velocity and the substrate coating thickness. Generally, a larger initial velocity poses a higher probability of cell damage, and a substrate coating can significantly reduce the cell mechanical damage severity.
3. Two important impact processes may occur during the cell droplet landing process after ejection: the first impact between the cell droplet and the substrate coating and the second impact between the cell and the substrate. It is assumed that the impact-induced cell damage depends not only on the magnitudes of stress, acceleration, and/or shear strain but also the cell loading history. In fact, the collective cell momentum change over the whole impact duration instead of peak values of stress, acceleration, and/or strain looks critical in determining the cell viability during cell direct writing.
4. For better understanding of cell damage during direct writing, future studies should apply realistic cell and hydrogel constitutive models, consider the mechanical damage during the cell droplet formation process (ejection), and include the possible process-induced thermal damage. Also, how to quantify the cell damage degree should be carefully addressed, validated, and interpreted.

Acknowledgment

The study was partially supported by the National Textile Center and the National Science Foundation (CMMI-0747959).

References

[1] Xu, T., Petridou, S., Lee, E. H., Roth, E. A., Vyavahare, N. R., Hickman, J. J., and Boland, T., 2004, "Construction of High-Density Bacterial Colony Arrays and Patterns by the Ink-Jet Method," Biotechnol. Bioeng., **85**(1), pp. 29–33.
[2] Xu, T., Jin, J., Gregory, C., Hickman, J. J., and Boland, T., 2005, "Inkjet Printing of Viable Mammalian Cells," Biomaterials, **26**, pp. 93–99.
[3] Odde, D. J., and Renn, M. J., 2000, "Laser-Guided Direct Writing of Living Cells," Biotechnol. Bioeng., **67**, pp. 312–318.
[4] Ringeisen, B. R., Kim, H., Barron, J. A., Krizman, D. B., Chrisey, D. B., Jackman, S., Auyeung, R. Y. C., and Spargo, B. J., 2004, "Laser Printing of Pluripotent Embryonal Carcinoma Cells," Tissue Eng., **10**(3–4), pp. 483–491.
[5] Barron, J. A., Ringeisen, B. T., Kim, H., Spargo, B. J., and Chrisey, D. B., 2004, Application of Laser Printing to Mammalian Cells, Thin Solid Films, **453–454**, pp. 383–387.
[6] Hopp, B., Smausz, T., Kresz, N., Barna, N., Bor, Z., Kolozsvari, L., Chrisey, D. B., Szabo, A., and Nogradi, A., 2005, "Survival and Proliferative Ability of Various Living Cell Types After Laser-Induced Forward Transfer," Tissue Eng., **11**(11/12), pp. 1817–1723.
[7] Ringeisen, B. R., Othon, C. M., Barron, J. A., Young, D., and Spargo, B. J., 2006, "Jet-Based Methods to Print Living Cells," Biotechnology, **1**, pp. 930–948.
[8] Young, D., Auyeung, R. C. Y., Piqué, A., Chrisey, D. B., and Dlott, D. D., 2001, "Time-Resolved Optical Microscopy of a Laser-Based Forward Transfer Process," Appl. Phys. Lett., **78**, pp. 3169–3171.
[9] Wang, W., Huang, Y., and Chrisey, D. B., 2007, "Numerical Study of Cell Droplet and Hydrogel Coating Impact Process in Cell Direct Writing," Trans. NAMRI/SME, **35**, pp. 217–223.
[10] LS-DYNA Theory Manual, 2006, Livermore Software Technology Corporation, Livermore, CA.
[11] Gingold, R. A., and Monaghan, J. J., 1977, "Smoothed Particle Hydrodynamics: Theory and Application to Non-Spherical Stars," Mon. Not. R. Astron. Soc., **181**, pp. 375–389.
[12] Lucy, L. B., 1977, "A Numerical Approach to the Testing of Fusion Process," Astron. J., **88**, pp. 1013–1024.
[13] Johnson, G. R., Stryk, R. A., and Neissel, S. R., 1996, "SPH for High Velocity Impact Computations," Comput. Methods Appl. Mech. Eng., **139**, pp. 347–373.
[14] Liu, M. B., Liu, G. R., Lam, K. Y., and Zong, Z., 2003, "Meshfree Particle Simulation of the Detonation Process for High Explosives in Shaped Charge Unlined Cavity Configurations," Shock Waves, **12**, pp. 509–520.
[15] Ellero, M., and Tanner, R. I., 2005, "SPH Simulations of Transient Viscoelastic Flows at Low Reynolds Number," J. Non-Newtonian Fluid Mech., **132**, pp. 61–72.
[16] Monaghan, J. J., and Gingold, R. A., 1983, "Shock Simulation by the Particle Method SPH," J. Comput. Phys., **52**, pp. 374–389.
[17] Stammen, J. A., Williams, S., Ku, D. N., and Guldberg, R. E., 2001, "Mechanical Properties of a Novel PVA Hydrogel in Shear and Unconfined Compression," Biomaterials, **22**, pp. 799–806.
[18] Vijayasekaran, S., Fitton, J. H. Hicks, C. R., Chirila, T. V., Crawford, G. J., and Constable, I. J., 1998, "Cell Viability and Inflammatory Response in Hydrogel Sponges Implanted in the Rabbit Cornea," Biomaterials, **19**(24), pp. 2255–2267.
[19] Young, C. D., Wu, J. R., and Tsou, T. L., 1998, "High-Strength, Ultra-Thin and Fiber-Reinforced pHEMA Artificial Skin," Biomaterials, **19**, pp. 1745–1752.
[20] Nam, K., Watanabe, J., and Ishihara, K., 2005, "Network Structure of Spontaneously Forming Physically Cross-Link Hydrogel Composed of Two-Water Soluble Phospholipid Polymers," Polymer, **46**, pp. 4704–4713.
[21] Wang, T., Turhan, M., and Gunasekaran, S., 2004, "Selected Properties of pH-Sensitive, Biodegradable Chitosan-Poly (Vinyl Alcohol) Hydrogel," Polym. Int., **53**, pp. 911–918.
[22] Roeder, B. A., Kokini, K., Sturgis, J. E., Robinson, J. P., and Voytik-Harbin, S. L., 2002, "Tensile Mechanical Properties of Three-Dimensional Type I Col-

lagen Extracellular Matrices With Varied Microstructure," ASME J. Biomech. Eng., **124**, pp. 214–222.
[23] Drury, J. L., Dennis, R. G., and Mooney, D. J., 2004, "The Tensile Properties of Alginate Hydrogels," Biomaterials, **25**, pp. 3187–3199.
[24] Lin, D. C., Yurke, B., and Langrana, N. A., 2004, "Mechanical Properties of a Reversible, DNA-Crosslinked Polyacrylamide Hydrogel," ASME J. Biomech. Eng., **126**, pp. 104–110.
[25] Lim, C. T., Zhou, E. H., and Quek, S. T., 2006, "Mechanical Models for Living Cells—A Review," J. Biomech., **39**, pp. 195–216.
[26] Malvern, L. E., 1969, *Introduction of the Mechanics of a Continuous Medium*, Prentice-Hall, Englewood Cliffs, NJ.
[27] Lanero, T. S, Cavalleri, O., Krol, S., Rolandi, R., and Gliozzi, A., 2006, "Mechanical Properties of Single Living Cells Encapsulated in Polyelectrolyte Matrixes," J. Biotechnol., **124**, pp. 723–731.
[28] Lysne, P. C., 1970, "A Comparison of Calculated and Measured Low-Stress Hugoniots and Release Adiabats of Dry and Water-Saturated Tuff," J. Geophys. Res., **75**, pp. 4375–4386.
[29] Liu, M. B., Liu, G. R., and Lam, K. Y., 2002, "Investigations Into Water Mitigation Using a Meshless Particle Method," Shock Waves, **12**, pp. 181–195.
[30] Barbee, K. A., 2005, "Mechanical Cell Injury," Ann. N.Y. Acad. Sci., **1066**, pp. 67–84.
[31] Serbest, G., Horwitz, J., Jost, M., and Barbee, K., 2006, "Mechanisms of Cell Death and Neuroprotection by Poloxamer 188 After Mechanical Trauma," FASEB J., **20**, pp. 308–310.
[32] Geddes-Klein, D. M., Schiffman, K. B., and Meaney, D. F., 2006, "Mechanisms and Consequences of Neuronal Stretch Injury In Vitro Differ With the Model of Trauma," J. Neurotrauma, **23**(2), pp. 193–204.
[33] Smith, A. E., Moxham, K. E., and Middelberg, A. P. J., 2000, "Wall Material Properties of Yeast Cells. Part II. Analysis," Chem. Eng. Sci., **55**, pp. 2043–2053.